Ordered vacancies in the fluorite and perovskite layers of the lanthanide BiLuWO6 phase by HREM

Loïc Patout, Claude Alfonso, Ahmed Charaï

Ordered vacancies in the fluorite and perovskite layers of the lanthanide $BiLuWO_6$ phase by HREM

Loïc Patout, Claude Alfonso & Ahmed Charaï

IM2NP-CNRS, Aix-Marseille Université, Avenue Escadrille Normandie Niemen, Marseille, F-13397, France

Keywords. Superstructure; cationic vacancies order; HREM projection symmetries; HREM and ED simulations

Abstract. The paper brings new information about the superstructure present in the monoclinic *A2/m* $BiLuWO_6$ crystal phase. Electron diffraction (ED) and high resolution electron microscopy (HREM) investigations in several crystal projections have highlighted the presence of cationic vacancies ordered in the fluorite and perovskite blocks. The order generates a doubling of the unit-cell parameter *b* and a lowering of the translation symmetries inside the lattice in agreement with the *P2* space group (SG).

1. Introduction

The lutetium tungstate Lu_2WO_6 crystallizes in a bilayer structure inside a monoclinic lattice of *P2/c* SG ***(Fig. 1a)***. The layer A is composed of edge-linked chains of LuO_8 dodecahedra and LuO_7 decahedra. In layer B, groups of LuO_8 dodecahedra join four adjacent WO_6 distorted octahedra **[1]**.

The bismuth tungstate Bi_2WO_6 is an archetypal $n = 1$ member of the Aurivillius family, which is structurally composed of alternating fluorite-like $(Bi_2O_2)^{2+}$ and perovskite-like $(A_{n-1}B_nO_{3n+1})^{2-}$ blocks where A is a large 12-coordinated cation and B is a small 6-coordinated cation **[2, 3]**. The perovskite-like blocks consist of corner-linked WO_6 octoahedra in a two-dimensional array sandwiched between two bismuth oxide layers ***(Fig. 1b)***. Bi_2WO_6 has three polymorphic phases as a function of the temperature with a ferro-paraelectric transition at highest temperature. The first structure transition from the $Pca2_1$ SG to a higher symmetry *B2cb* occurs at about 660°C keeping essentially the same connectivity. Then around 960°C corresponding to the ferroelectric Curie point, the $[WO_4]^{2-}$ layers are built in a *A2/m* symmetry from edge-linked chains of octahedra along the *a*-axis and a corner-sharing along the *b*-axis. As conventional for Aurivillius phases, the stacking axis normal to the layers is defined as the *c*-axis of the *A2/m* structure **[4, 5]**. Although the chemical composition remains the same leading to some structural similarities, there is no immediate relationship between the two polymorphs whose symmetry groups are not group-subgroup related. This kind of phase transition with breaking and reforming of nearest-neighbor coordination bonds are necessarily reconstructive **[6]**. In addition to the attractive fundamental aspect concerning the phase transitions, the Aurivillius phase materials possess interesting physical properties in multiferroics **[7, 8]**. They have been studied for their dielectric and ferroelectric properties like resonators and antennae **[9]**, also as electrolytes in solid oxide fuel cells **[10, 11]**. The sandwich-type layered structures favors an efficient separation of electron-hole pair due to the internal electric field formed within the layers, that plays a crucial role in photocatalysis **[12-15]**. In the case of Bi_2WO_6, doping with RE (rare earth) ions is associated with f-f transitions improving the light absorption capacity from UV, visible and IR for efficient photocatalysis **[16-18]**.

The photoluminescence properties of the system $Bi_{2-x}Lu_xWO_6$ ($0.1 \leq x \leq 1$) were investigated under monochromatic UV-laser light irradiation. The increase in integrated intensity with the x value was related to the formation of the monoclinic structure induced by the bismuth substitution in lutetium **[19]**.

In a previous study, a mixed phase of bismuth lutetium tungstate $BiLuWO_6$ was solved in the same *A2/m* monoclinic SG than the paramagnetic high temperature (HT) Bi_2WO_6 crystal phase **[20]**. This is in agreement with a $BiREWO_6$ phase synthesized at solid-state for all REs from La to Lu **[21]**. However, electron diffraction investigations showed additional reflections of weak intensity, as shown for the [001] pattern, ***(Fig. 2a, b)*** revealing the presence of a *2b*-superlattice. The reflection conditions were in agreement with a monoclinic primitive system but didn't allow to dissociate between the *P2* or *P2/m* space groups.

In the present paper, HREM and ED investigations allowed to identify the symmetries and the origin of the superstructure. The three main zone axes [001], [100] and [010] as well as other intermediate orientations [0*vw*], [*u*0*w*] and [*uv*0] allowed to compare experimental ED and HREM projections with simulations done from several crystal models described further.

2. Experimental

Bismuth lutetium tungstate was prepared using a solid state reaction process, which is a commonly adopted synthesis to elaborate multicomponent oxides. Appropriate amounts of lutetium oxide Lu_2O_3 (Fluka Chemica > 99%), bismuth oxide Bi_2O_3 (Fluka Chemica > 99%) and tungsten oxide WO_3 (Fluka Chemica > 99%) were mixed and milled thoroughly in the stoichiometric ratios in an agate mortar. Then, the as prepared composition was heated at 1000°C for 15h. The sample was cooled in the furnace from the calcination temperature to room temperature, leading to the desired phase $BiLuWO_6$ under polycrystalline form.

The electron microscopy specimen was prepared by crushing a small amount of the powder in an agate mortar and dispersing it in methanol. The suspension was then dropped on a holey carbon film supported by a copper grid.

HREM images were carried out with a Field Emission Gun FEI Titan Cs-corrected transmission electron microscope (TEM) operating at 200 kV allowing a point-to-point resolution of 1Å. Selected area ED patterns and EDS analyses were acquired using a LaB_6 FEI Tecnai TEM at 200 kV equipped with a SDD Oxford Xmax80 spectrometer. The atomic models were created in CrystalMaker then exported to the TEM software package JEMS for HREM, electron and X-Ray diffraction simulations **[22].**

The electron microscopy simulations were done using the Blochwave theory with the following microscope settings: acceleration voltage (E_0 = 200 kV), chromatic (C_c = 1mm) and spherical (Cs = -0.05 mm) aberration coefficients, defaults defocus (d_f = -13.72 nm), gun energy spread ΔE_s = 0.6 eV, default objective lens current (ΔI = 0.1 ppm) and voltage (ΔV = 1 ppm) stabilities.

3. Results

3.1. EDS

A quantitative EDS analysis was estimated using the L-peaks of the three cationic elements with the k_L-factor theoretical values k_L(Bi) = 2.61, k_L(Lu) = 2.205 and k_L(W) = 2.268. The measurements done on five different grains gave the following concentration values in atomic percentage Lu (33.5±1.6), Bi (32.3±1.6) and W (34.2±1.6) therefore the stoichiometry $Bi_{0.94\pm0.05}Lu_{0.98\pm0.05}W_{1\pm0.05}$.

3.2. HREM

3.2.1. Identification of the superstructure symmetry

As for $BiNdWO_6$ **[23]**, $BiLuWO_6$ was refined in the *A2/m* SG from X-Ray experiments **[20]**. In both cases, the fact that y_w and z_w coordinates were set to positions very slightly different from 0.5 generates a splitting of W atoms in a same site due to the SG translation symmetries. Therefore, as a starting point of the present study, we have fixed these coordinates at the specific position 0.5 in order to get a lattice with only one single W atom in the corresponding sites ***(Table 1)***.

Another point concerns the weak contribution of the oxygen atoms on the electron structure factors as shown in the HREM simulations ***(Fig. 3)***. Just a small variation of the reflections amplitude and light additional contrasts could be observed, the oxygen elements were therefore not taken into account for the simulations in the rest of the study.

In the [100] experimental HREM image ***(Fig. 4a)***, the columns assigned to fluorite and perovskite blocks could be distinguished with specific contrasts. However, the alternation at each peak along the perovskite chains was not observed in the corresponding calculation of the *A2/m* structure ***(Fig. 3)***. Green arrows were set on the brightest peaks forming herringbone-shaped motifs for which the mirror plane symmetry is perpendicular to the *c*-axis. This symmetry in agreement with a *p11m* projection is the one of a *P2 (unique b-axis)* SG for the [100] zone axis. A *P2/m* SG would have shown a *p2mm* symmetry projection namely with an additional mirror plane perpendicular to the *b*-axis **[24]**.

3.2.2. Origin of the superstructure

The lowering of symmetry from *A2/m* to *P2* concerns a cationic order in the perovskite blocks according to the HREM image in [100] projection. In order to model the cationic arrangement in the superstructure, other experimental HREM images were recorded in the [0-10] ***(Fig. 4f)***, [110] ***(Fig. 5a)*** and [-101] ***(Fig. 5f)*** zone axes. It is important to note that the [110] zone axis of the *A2/m* system is indexed [210] in the *2b*-superlattice of *P2* SG (*2b-P2*), that will be

explained in the next section. The images were then compared with simulations done from different crystal models described here after.

A first model was created from the *A2/m* $BiLuWO_6$ *1x2x1*-supercell ***(Fig. 6a)*** in which the cationic positions were translated in the *2b-P2* superlattice ***(Fig. 6b)***. Then, two other models were built with two specific W columns alternating along the *b*-axis in order to get HREM simulations with same contrast features than the ones obtained in the [100] experimental image. The second model was therefore designed with W columns one of which completely filled and another one with a missing atom ***(Fig. 6c)***. In the third model, W atoms have two different occupancy values, namely 1 and 0.8 in each respective column ***(Fig. 6d)***. An optimized model designed from the following results will be presented at the end of the section. The crystal data of the different models are summarized in ***Table 2***.

All experimental HREM images make appear the perovskite columns with contrast alternations at each peak which are representative of the superstructure. The brightest peaks pointed out with green arrows form motifs that were compared with simulations done for each model. The projected thickness values were chosen as the smallest ones from which a qualitative contrast ratio between the fluorite and perovskite blocks was similar with the experimental images. For [100], the herringbone-shaped motifs with alternation of contrast along *b* were found for the models 2 and 3 ***(Fig. 4c, d)***, but not for the model 1 ***(Fig. 4b)***. For [0-10], the diamond-shaped motifs with alternation of contrast along *a* were found only for the model 2 ***(Fig. 4h)***. For [210], the parallelogram-shaped motifs with alternation of contrast ***(Fig. 5a)*** along *a+b* were also found only for the model 2 ***(Fig. 5c)***.

At this stage, the HREM simulations done from the model 2 were the most coherent regarding the experimental projections. However for [-101], the contrast alternations along *b* whose the brightest dots form zigzag motifs along *a+c* in the experimental HREM image ***(Fig. 5f)*** were different in the simulation ***(Fig 5h)***. Indeed, the peaks pointed out with red arrows should

show an intensity similar to the brightest ones. Also, the simulation done for the [210] projection ***(Fig. 5c)*** didn't show the contrast alternation at each peak along *a*+*b* in the columns assigned to the Bi/Lu planes pointed out with blue arrows in the experimental HREM image ***(Fig. 5a)***. A last crystal lattice (model 4) was therefore optimized always with two specific W columns alternating along the *b*-axis allowing a good correlation between the simulated and experimental image for the [100] projection. Each W column has one atom with a specific occupation value, namely 0.8 and 0.9 ***(Fig. 6e)***. The same features as the ones obtained with the model 2 were then found in the perovskite columns for the [100] ***(Fig. 4e)***, [0-10] ***(Fig. 4j)*** and [210] ***(Fig. 5e)*** projections. Furthermore, for [-101] (***Fig. 5j***), the contrast alternation at each peak along *b* was more obvious in the columns containing brightest dots. In addition to the good agreement between the simulated and the experimental HREM images, the last model shows a stoichiometry of the W atoms closer to the one estimated by the EDS quantification as compared with the models 2 and 3 ***(Table 2)***.

In the previous models, the occupation of the Bi/Lu cationic sites fixed at 0.5 showed one column of peaks with a constant brightness along *a*+*b* in the simulated [210] HREM projection pointed out with blue arrows ***(Fig. 5b-d)***. This feature was also observed by reducing and increasing of a same offset value the occupation of the different chemical elements, for example Bi0.4 and Lu0.6. However, the introduction of cation vacancies in some specific Bi sites with an occupation value of 0.46 allowed the contrast alternation in the mentioned columns ***(Fig. 5j)***. Bi was chosen as minority element regarding the estimation of the EDS quantification. The optimized model was chosen for ED simulations in order to confront the results with the experimental patterns. We will then discuss about the interest of HREM and ED analyses in the characterization of this kind of superstructure and the complementarity with the X-Ray and neutron diffraction techniques.

3.3. Diffraction

3.3.1. Electron diffraction

ED patterns were recorded in other zone axes than the ones used for the HREM analyses, from [001] to the [100] and [010] directions, in order to confirm the *2b-P2* superstructure. All patterns were compared with two simulated patterns, one for the *A2/m* structure and another one for the superstructure model optimized in the previous section (model 4). It is important to note that the doubling of the *b*-axis generates some differences between the index notation assigned to the structure and the one of the superstructure. Therefore, the indices of the zone axes don't change for the [*u*0*w*] directions as we can note for the [102] ***(Fig. 7a-c)*** pattern. On the contrary, it differs for the [0*vw*] and [*uv*0]; [0-11] becoming [0-12] ***(Fig. 7d-f)***, while [110] becomes [210] as observed in the previous section ***(Fig. 5a-e)***. Other patterns in supplementary information show the same features; the indices of the [-101] zone axis remain the same for the *2b-P2* superstructure, while [021] becomes [011].

The [001] pattern ***(Fig. 2a)*** shows reflections belonging to different Laue zones represented in red (Zero Order: ZOLZ) and green colors (First Order: FOLZ) in the simulations ***(Fig. 2b-c)***. The same periodicity and the shift along *b** of the strong reflections between the ZOLZ and the FOLZ are in agreement with the *A2/m* structure ***(Fig. 6b)***.

For the [*u*0*w*] and [0*vw*] zone axes, HOLZ reflections are present to the center of the ZOLZ in the [102] and [0-12] patterns ***(Fig. 7)***. This is explained by the proximity of these zone axes with the longest *c*-axis. The short distance between the strata in the reciprocal space allows to the Ewald sphere to intercept several orders that generates the presence of HOLZ reflections in the pattern. This feature was already observed in the case of the lanthanide crystal phase $Ce_{10}W_{22}O_{81}$ for patterns acquired close to the longest *b*-axis. **[25, 26]**.

For each simulated pattern, we have superposed the smallest geometric motifs for which the corners were set on reflections. The motifs were then reported on the experimental patterns.

The result shows that the patterns are formed by strong and weak reflections belonging to the structure and the superstructure respectively. The experimental and simulated patterns were in good agreement and all weak reflections could be indexed and attributed to the *2b-P2* superstructure.

3.3.2. X-Ray diffraction (XRD)

The presence of heavy and light atoms in oxide materials makes essential the X-ray and neutron scattering methods to refine a structure and understand the observed properties. The neutrons are more sensitive to lighter oxygen atoms and hence can help to determine their precise position. Combined with X-rays, the lattice parameters as well as positions, occupancies and thermal parameters of all atoms in the structure can be refined. For $Bi_{0.7}Yb_{1.3}WO_6$ and several related compositions of the *A2/m* structure types, powder neutron diffraction Rietveld refinements suggested a model involving a two-fold rotational disorder of the WO_6 octahedra around the *a*-axis with the tungsten and some of the oxygen atoms in a positional disorder **[23].** The monoclinic phase of $Bi_{2-x}Y_xWO_6$ nanoparticles obtained by a sol-gel method was refined from X-ray diffraction Rietveld refinements using both ordered (HT-Bi_2WO_6) and disordered ($BiNdWO_6$) models which yields a similar fit **[27]**. A crystal structure of hydrothermally synthesized monoclinic phase of $BiREWO_6$ (RE = Eu and Tb) nanorods was established by a combined Rietveld refinement of synchrotron and neutron data by using the same ordered and disordered models. The local structure analysis using high Q data by neutron pair distribution function (PDF) method in short (r = 1.5-5A) and medium (r = 1.5-11A) ranges concluded that ordered model was suitable for these nanomaterials **[2]**. Here, concerning $BiLuWO_6$, XRD diagrams were simulated using the refinement done in the *A2/m* structure ***(Fig. 8a)*** and the *2b-P2* superstructure optimized model ***(Fig. 8b)***. In each case, the oxygen atoms were not taken into account. Despite a similar global feature of the two diagrams, intensity differences could be noticed as well as absence of peaks in the case of

the superstructure. The comparison between the simulated diagrams with the experimental one **[20]** suggests that the real model is actually closer to the A2/m average structure. However, the additional reflections in ED and the contrast alternations in HREM can not be assigned to ordered or disordered models refined in the A2/m structure. The association of the electron and X-ray data allows to propose a model of the $BiLuWO_6$ crystal phase defined in a *A2/m* average structure with cation vacancies partially ordered in a *2b-P2* SG superstructure. The electron data bring a new qualitative structural information usefull for further quantitative data.

Conclusion

The aim of this paper was to clarify certain issues regarding the superstructure present in the *A2/m* $BiLuWO_6$ crystal phase from 3D electron data. ED investigations were in agreement with a lowering of symmetry to the non-centrosymmetric *P2* space group doubling the *b* unit-cell parameter. HREM investigations in other zone axes validated the superstructure symmetry and confirmed a partial order of the cation vacancies in the perovskite blocks. One zone axis of low symmetry, here [210] also shows this feature in the fluorite blocks. A model containing alternation of cations with different occupancy values in specific sites improves the correlation between experimental and simulated HREM projections. Therefore, this qualitative result combining ED and HREM investigations by TEM shows the complementarity of the electron data with X-ray and neutron scattering methods. Particularly, the overlap problems in XRD are overcome with ED techniques for which the high quantity of reflections can be unambiguously indexed. Furthermore, the presence of the phase information in the HREM images makes electron microscopy a non-negligible choice, especially using an instrument equipped with a FEG and a Cs-correction, to solve compounds containing ordered cationic defects.

Ackowledgments

We thank CP2M - Aix-Marseille University (Centre Pluridisciplinaire de Microscopie électronique et de Microanalyse), namely the Research Engineers Christian Dominici, Thomas Neisius, Andrea P. Campos and Martiane Cabié, for technical support.

References

[1] Zhang, Z., Zhang, H., Duan, C., Yuan, J., Wang, X., Xiong, D., Chen, H., Zhao, J., J. Alloys Compd., 466, 1–2 (2008) 258-263.

[2] McDowell, N. A., Knight, K.S., Lightfoot, P., Chem. Eur. J., 12, 5 (2006) 1493-1499.

[3] Shanbogh, P. P., Raghunathan, R., Swain, D., Feygenson, M., NeueFeind, J., Plaisier, J., Narayana, C., Rao, A., and Sundaram, N. G., ACS Appl. Mater. Interfaces, 10, 42 (2018) 35876-35887.

[4] Djani, H., Bousquet, E., Kellou, A., Ghosez, P., Phys. Rev. B 86 (2012) 054107.

[5] Voronkova, V. I., Kharitonova, E. P., Rudnitskaya, O. G., J. Alloys Compound., 487, 1-2 (2009) 274-279.

[6] Dmitriev, V. P., Rochal, S. B., Gufan, Yu. M., Toledano, P., Phys. Rev. Lett., 60, 19 (1988) 1958-1961.

[7] Sharma, N., Kennedy, B. J., Elcombe, M. M., Liu, Y., Ling, C. D., J. Phys.: Condens. Mater., 20, 2 (2007) 025215.

[8] Birenbaum, A. Y., Ederer, C., Phys. Rev. B 90, 21 (2014) 214109.

[9] Rocha, G. N., Melo, L. F. L., da Silva, M. A. S., Silva, P. V. S., Sombra, A. S. B., Fechine, P. B. A., Microwave Opt. Technol. Lett. 54 (2012) 18-23.

[10] Kendall, K. R., Navas, C., Thomas, J. K., zur Loye H.-C., Chem. Mater., 8, 3 (1996) 642-649.

[11] Azad, A. M., Larose, S., Akbar, S. A., J. Mater. Sci., 29 (1994) 4135-4151.

[12] Zhang, R., Dai, Y., Lou, Z., Li, Z., Wang, Z., Yang, Y., Qin, X., Zhang, X., Huang, B., CrystEngComm., 16 (2014) 4931-4934.

[13] Huang, H., He, Y., Li, X., Li, M., Zeng, C., Dong, F., Du, X., Zhang, T., Zhang, Y., J. Mater. Chem. A, 3 (2015) 24547-24556.

[14] Huang, H., Reshak, A. H., Auluck, S., Jin, S., Tian, N., Guo, Y., Zhang, Y., J. Phys. Chem. C, 122, 5 (2018) 2661-2672.

[15] Liu, H., Yuan, J., Shangguan, W., Teraoka, Y., J. Phys. Chem. C, 112, 23 (2008) 8521-8523.

[16] Tian, Y., Zhang, L., Zhang, J., J. Alloys. Compd., 537 (2012) 24-28.

[17] Tian, N., Zhang, Y., Huang, H., He, Y., Guo, Y., J. Phys. Chem. C, 118, 29 (2014) 15640-15648.

[18] Huang, H., Liu, K., Chen, K., Zhang, Y., Zhang, Y. Wang, S., J. Phys. Chem. C, 118, 26 (2014) 14379- 14387.

[19] Ait Ahsaine, H., Ezahri, M., Benlhachemi, A., Bakiz, B., Villain, S., Valmalette, J.-C., Guinneton, F., Arab, M., Gavarri, J.-R., RSC Adv., 5 (2015) 96242-96252.

[20] Ait Ahsaine, H., Taoufyq, A., Patout, L., Ezahri, M., Benlhachemi, A., Bakiz, B., Villain, S., Guinneton, F., Gavarri, J.-R., J. sol. State. Chem. 218 (2014) 124-130.

[21] Watanabe, A., Mater. Res. Bull., 15, 10 (1980) 1473-1477.

[22] Stadelmann, P. A., Ultramicroscopy, 21, 2 (1987) 131-145.

[23] Berdonosov, P. S., Charkin, D. O., Knight, K. S., Johnston, K. E., Goff, R. J., Dolgikh, V. A., Lightfoot, P., J. sol. State. Chem., 179, 11 (2006) 3437-3444.

[24] International Tables for Crystallography, vol. A Space-group symmetry, edited by Th. Hahn, Fifth edition, published by Kluwer Academic Publishers Dordrecht/Boston/London 2002.

[25] Patout, L., Jacob, D., Arab, M., Pereira de Souza, C., Leroux, Ch., Acta Cryst. B 70 (2014) 268-274.

[26] Patout, L., Hallaoui, A., Neisius, T., Campos, A. P. C., Dominici, C., Alfonso, C., Charaï, A., J. Appl. Cryst. 51 (2018) 344-350.

[27] Pasternak, S., Levy, D., Paz, Y., Pokroy, B., CrystEngComm., 18 (2016) 6464-6470

Figures

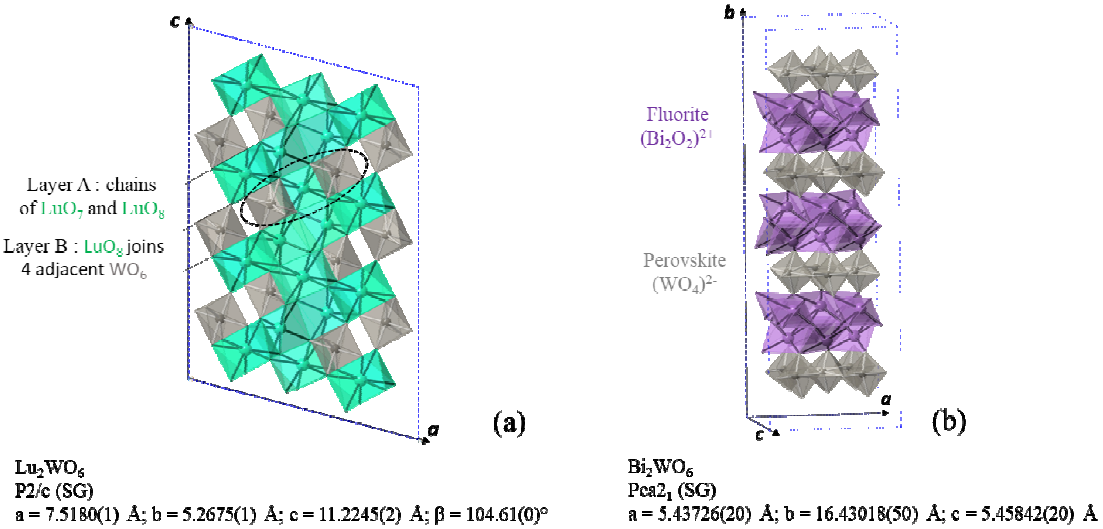

Figure 1: Representations of the Lu_2WO_6 bilayer structure (a) and the Bi_2WO_6 structure composed of alternating fluorite-like $(Bi_2O_2)^{2+}$ and perovskite-like $(WO_4)^{2-}$ blocks (b).

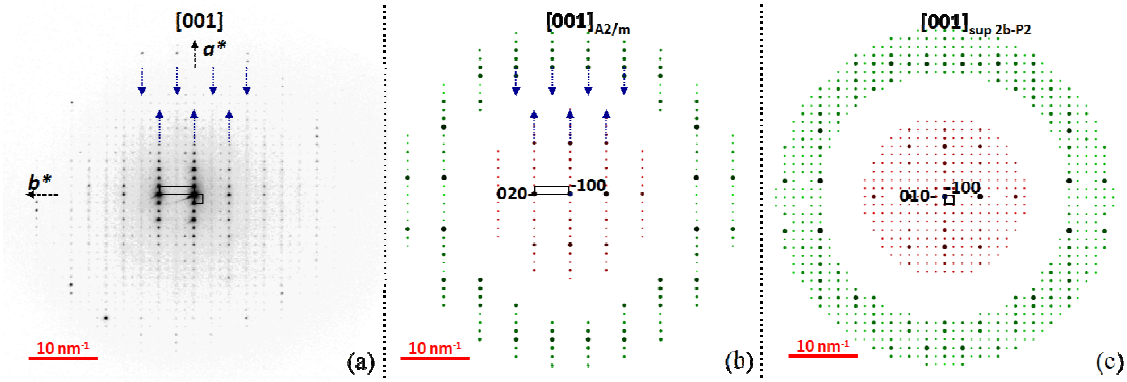

Figure 2: Experimental ED pattern of the $BiLuWO_6$ crystal phase in [001] zone axis (a). ED pattern calculated for the *A2/m* structure showing the same periodicity and the shift along ***b**** of the ZOLZ (red) and FOLZ (green) reflections (b). ED pattern calculated for the *2b – P2* superstrucure showing the additional columns of reflections (c).

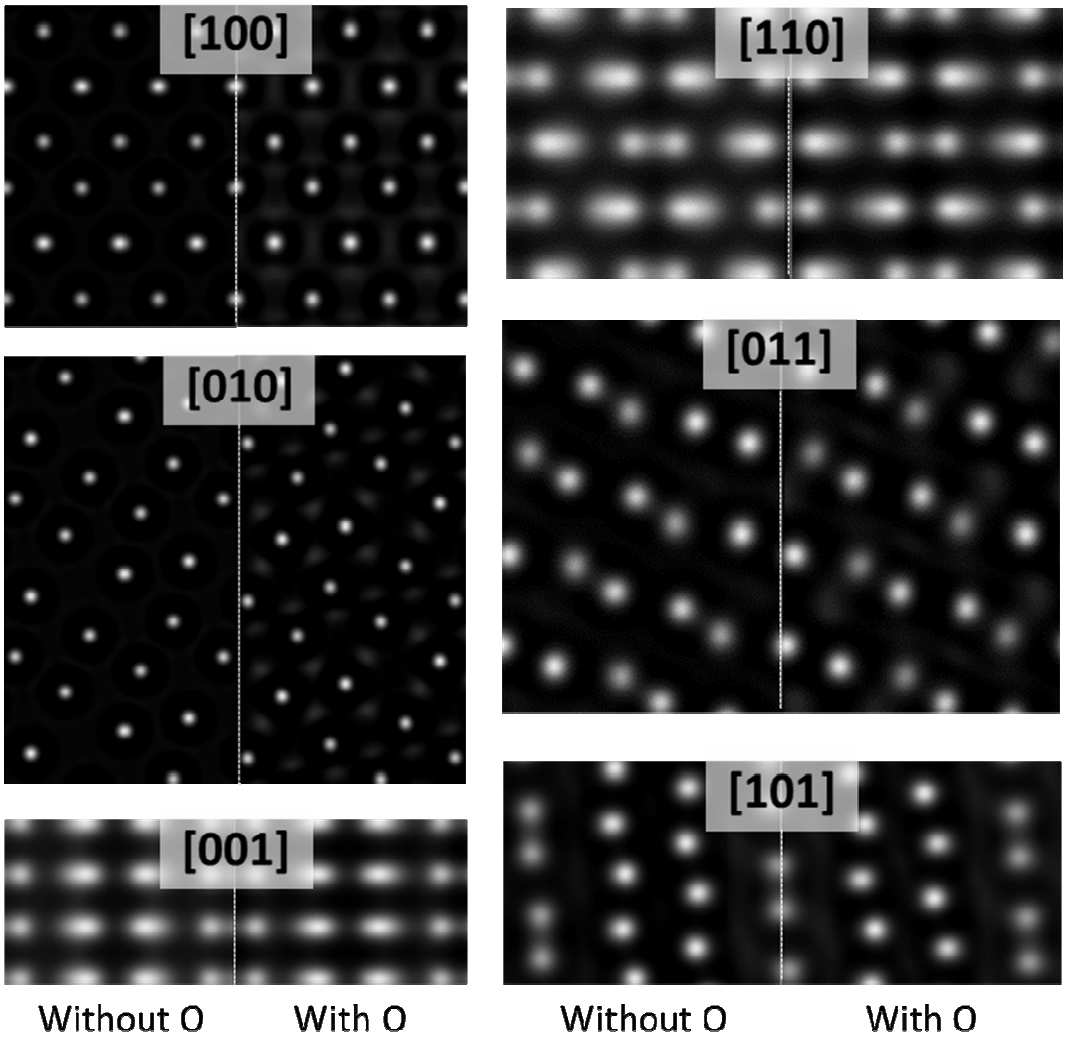

Figure 3: HREM projections calculated with E_0 = 200 kV for the *A2/m* $BiLuWO_6$ structure, highlighting the weak contribution of the oxygen elements.

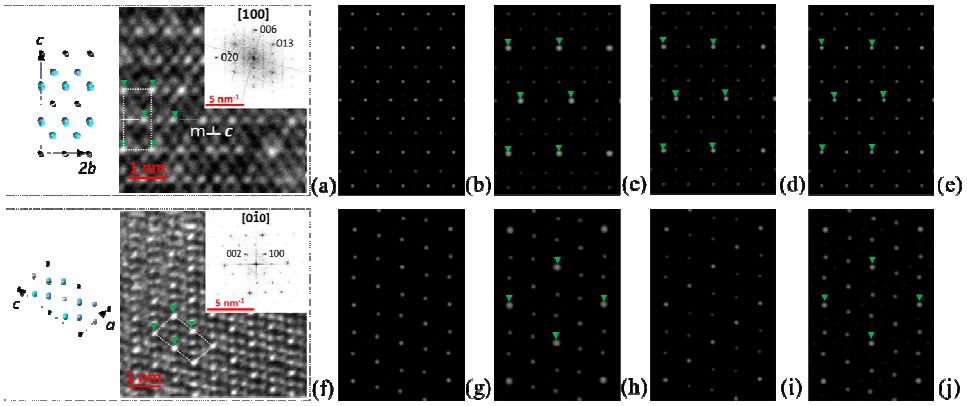

Figure 4: Experimental HREM images and corresponding power spectra (insert) in [100] and [0-10] projections (a, f). Simulated images for the model 1 (b, g), model 2 (c, h), model 3 (d, i) and model 4 (e, j). The calculations were done with 278 reflections and a thickness t = 6 nm for [100]; 298 reflections and t = 5 nm for [0-10].

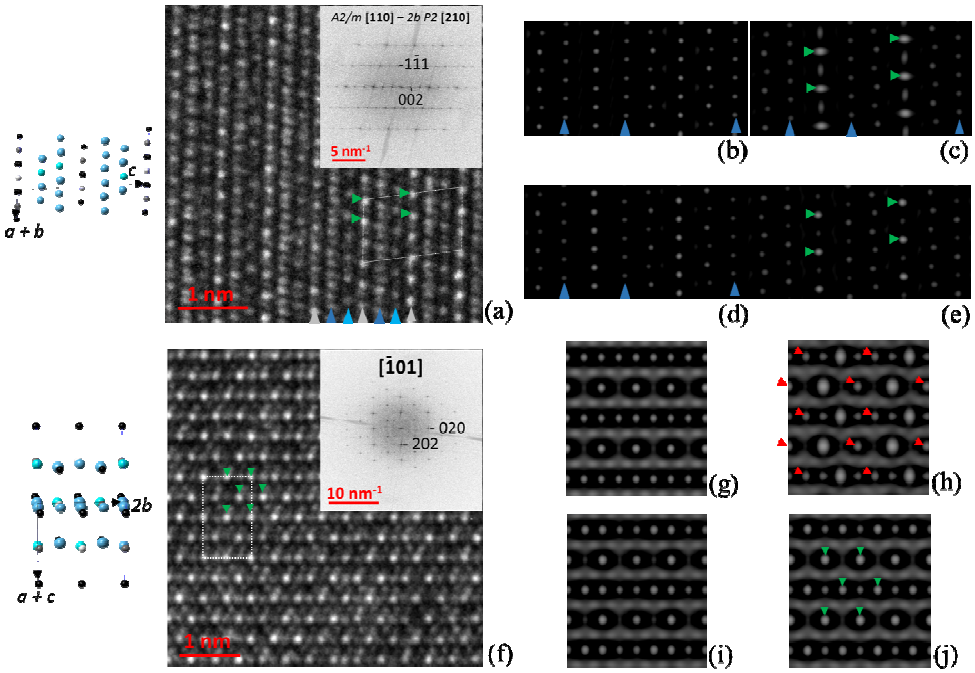

Figure 5: Experimental HREM images and corresponding power spectra (insert) in [210] and [-101] projections (a, f). The grey and blue arrows point to W and Bi/Lu columns respectively (f). Simulated images for the model 1 (b, g), model 2 (c, h), model 3 (d, i) and model 4 (e, j). The calculations were done with 266 reflections and a thickness t = 10.5 nm for [-101]; 256 reflections and t = 11.25 nm for [210].

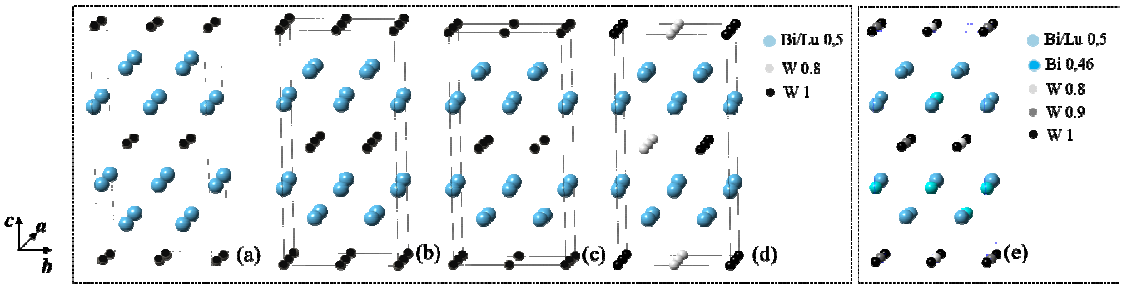

Figure 6: Representation of the different models used for the HREM simulations: *A2/m* $BiLuWO_6$ in 1x2x1 supercell (a); *P2* - $BiLuWO_6$ superstructure: models 1 (b), 2 (c), 3 (d) and 4 (e). The translation of the cations from *A2/m* to *P2* changes the origin.

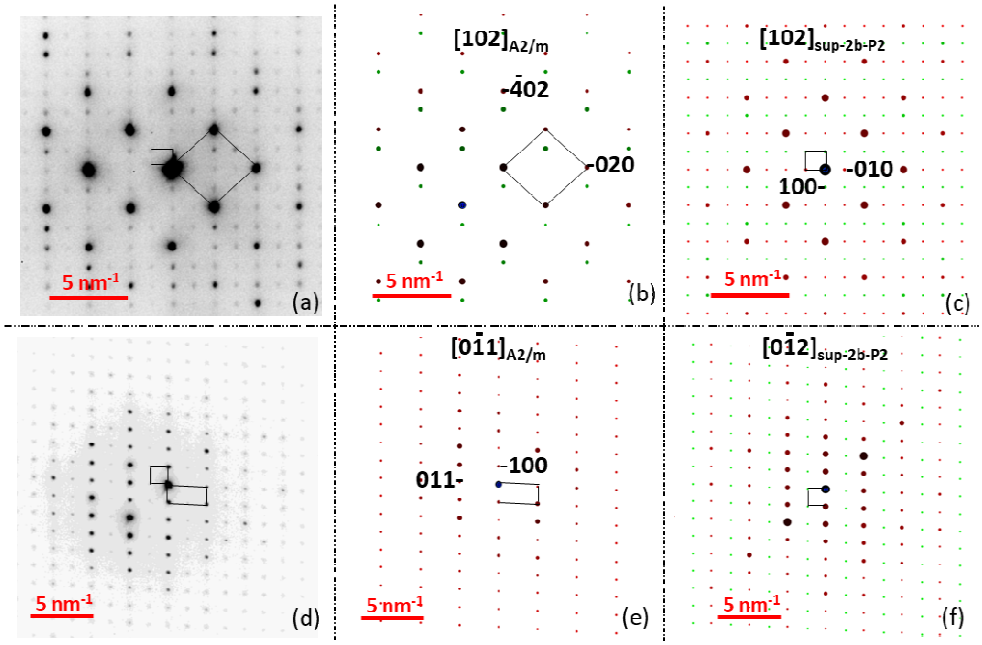

Figure 7: Experimental ED patterns of the $BiLuWO_6$ crystal phase (a, d) with the corresponding simulations for the *A2/m* structure (b, e) and the *2b – P2* superstructure (c, f). The superstructure patterns were calculated using the multibeam dynamical calculation with t = 32 nm (c) and t = 22 nm (f).

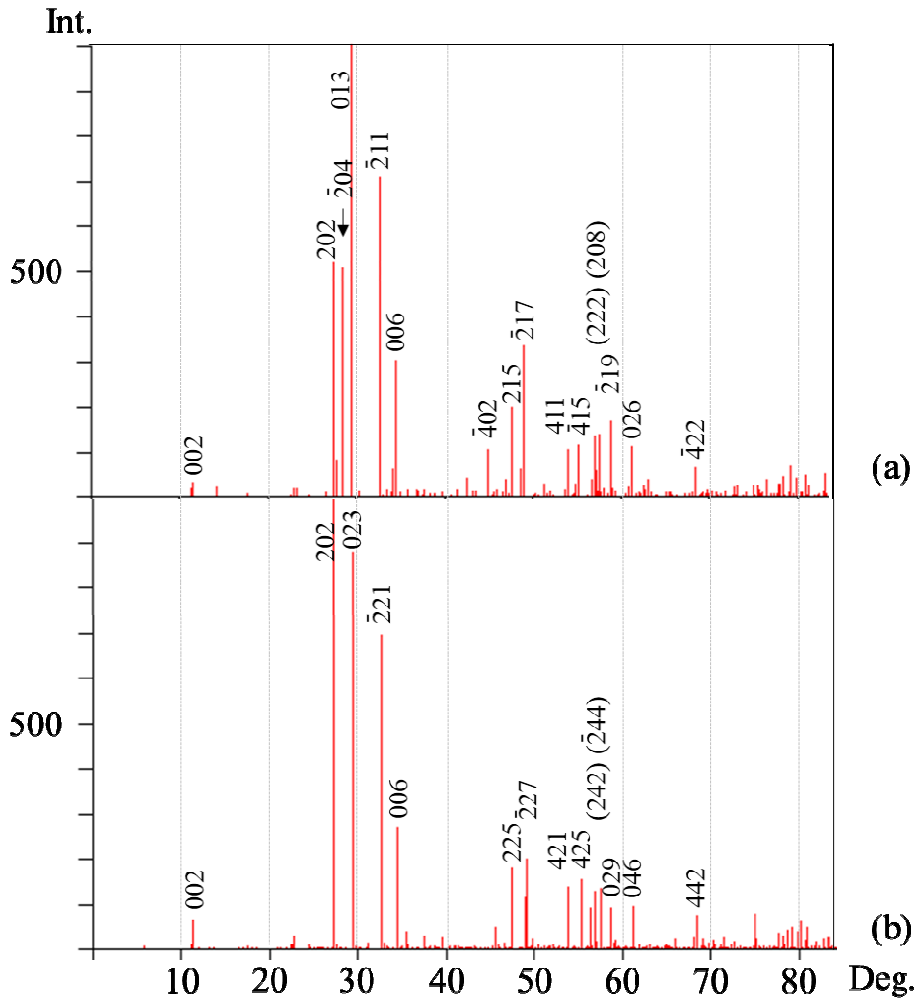

Figure 8: X-Ray diagrams simulated for the *A2/m* structure (a) and the *2b-P2* superstructure (b). The peak (-204) pointed out in (a) is not present in (b).

A2/m (SG)
a = 8.0830(1) Å; b = 3.7238(1) Å; c = 15.9493(2) Å; β(a,c) = 102.634(2)°

Atoms	x/a	y/b	z/c
Bi/Lu[a]	0.9224(2)	0	0.3315(2)
Bi/Lu[a]	0.3960(2)	0	0.3170(2)
W	0.2951(3)	0.4792(3)*	0.4925(3)*
O(1)	*0.1188*	*0*	*0.2489*
O(2)	*0.3640*	*0.5*	*0.2338*
O(3)[b]	*0.3224*	*0*	*0.5284*
O(4)[b]	*0.5068*	*0.438*	*0.5745*
O(5)[b]	*0.1709*	*0.414*	*0.5669*
O(6)[b]	*0.1664*	*0.609*	*0.3992*
O(3a)[b]	*0.2978*	*0*	*0.4628*

[a] Occupancy factor for Bi/Lu fixed at 50/50
[b] 50% Occupancy for oxygen atoms
* Adjusted to 0.5 for ED and HREM simulations

Table 1: Structural parameters refined for the *A2/m* monoclinic $BiLuWO_6$ crystal phase **[20]**.

P2 (SG)
a = 8.0830(1) Å b = 7.4476(2) Å c = 15.9493(2) Å β(a,c) = 102.634(2)°

Atoms	x/a	y/b	z/c	Occupancy model 1 BiLuW	model 2 $BiLuW_{0.75}$	model 3 $BiLuW_{0.9}$	model 4 $Bi_{0.5}LuW_{0.5}$
Bi/Lu	0.6774(7)	0	0.3315(7)	0.5	0.5	0.5	0.5
Bi/Lu	0.1460(2)	0	0.3170(2)	"	"	"	0.46/0.5
Bi/Lu	0.6724(2)	0.5	0.3315(2)	"	"	"	0.5
Bi/Lu	0.1460(2)	0.25	0.8170(2)	"	"	"	0.46/0.5
Bi/Lu	0.1460(2)	0.75	0.8170(2)	"	"	"	0.46/0.5
Bi/Lu	0.6460(2)	0.25	0.8170(2)	"	"	"	0.5
Bi/Lu	0.6460(2)	0.75	0.8170(2)	"	"	"	0.5
Bi/Lu	0.1460(2)	0.5	0.3170(2)	"	"	"	0.46/0.5
W	0	0	0	1	1	1	1
W	0.5	0.5	0	"	0	0.8	0.8
W	0.5	0.75	0.5	"	1	0.8	0.9
W	0	0.25	0.5	"	1	1	1
W	0.5	0.25	0.5	"	0	1	0.8
W	0.5	0	0	"	1	1	0.9
W	0	0.75	0.5	"	1	0.8	1
W	0	0.5	0	"	1	0.8	1

Table 2: Structural parameters refined for the *2b-P2* superstructure in four models.

Supplementary materials

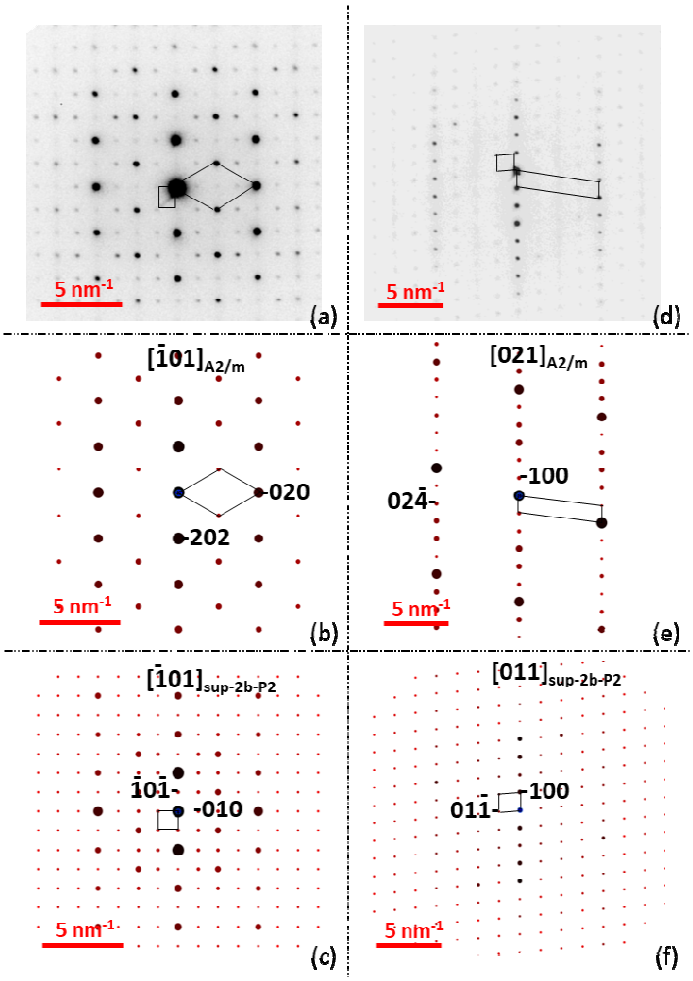

Figure: Experimental ED patterns of the $BiLuWO_6$ crystal phase (a, d) with the corresponding simulations for the *A2/m* structure (b, e) and the *2b – P2* superstructure (c, f). The superstructure patterns were calculated using the multibeam dynamical calculation with t = 20 nm (c) and t = 77 nm (f).